IEEE Access
Multidisciplinary | Rapid Review | Open Access Journal

Received February 10, 2020, accepted March 3, 2020, date of publication March 6, 2020, date of current version March 18, 2020.

Digital Object Identifier 10.1109/ACCESS.2020.2978906

Seamless Integration of Active Antenna With Improved Power Efficiency

YUNLONG LU[1], QING LIU[1], YI WANG[2], (Senior Member, IEEE), PETER GARDNER[2], (Senior Member, IEEE), WANG HE[1], YI CHEN[1], JIFU HUANG[1], AND TAIJUN LIU[1], (Senior Member, IEEE)

[1]Faculty of Electrical Engineering and Computer Science, Ningbo University, Ningbo 315211, China
[2]School of Engineering, University of Birmingham, Birmingham B15 2TT, U.K.

Corresponding authors: Yunlong Lu (luyunlong@nbu.edu.cn) and Taijun Liu (liutaijun@nbu.edu.cn)

This work was supported in part by the National Key R&D Program of China under Project 2018YFB1802100, in part by the National Natural Science Foundation of China under Project 61801252, Project 61631012, Project U1809203, and Project 61971250, and in part by the K. C. Wong Magna Fund in Ningbo University.

ABSTRACT Loss reduction to improve the power efficiency in active integrated antenna (AIA) is a key design drive. This paper first analyzes the loss mechanism in a convention AIA structure. A new integration scheme of a GaN power amplifier (PA) transistor with an antenna without using any output matching network (OMN) and harmonic tuning network (HTN) is then proposed to construct a seamlessly integrated AIA. This is achieved by a novel design of a slot antenna with optimized input impedance at its fundamental frequency as well as for harmonic tuning, which essentially absorbs the OMN and HTN functions in the conventional Class-F power amplifier design. By eliminating these passive networks between the transistor and the antenna, the associated insertion and mismatch losses as well as the overall circuit size are reduced. For verification, two prototypes are designed, fabricated and measured, one with the integrated design and the other with a conventional design for comparison. Both AIAs operate between 3.4 and 3.6 GHz. Experimental results show that the power-added efficiency (PAE) of the seamlessly integrated AIA is over 52% within the operating band. Compared with the conventional cascaded design of a PA and an antenna, the PAE is improved by 14.2%.

INDEX TERMS Amplifier integrated antenna, active antenna, Class-F power amplifier, loss reduction, seamless integration.

I. INTRODUCTION

The fast-growing wireless sensor network (WSN) technologies require numerous distributed low-power sensor nodes (SNs) to collect and transmit physical and environmental data [1]–[4]. Battery-powered SNs usually have limited lifetime and replacing batteries would require extensive human effort especially in hazard circumstances [5], [6]. Radio frequency (RF) signal based microwave power transfer (MPT) with omnidirectional power radiation has emerged as a perpetual and cost-effective solution to power randomly distributed large-scale wireless sensor networks over the distance and in an undisruptive way [7]–[12].

Compact high-efficiency transmitter is highly desired for MPT systems. Amplifier integrated antenna (AIA) is an attractive active antenna technology for front-end miniaturization [13]–[16]. AIAs have also been proposed for other wireless systems [17]–[20], such as radar, imaging and satellite communications.

Various methods have been developed to design AIAs. A conventional way is to design the high-efficiency power amplifier (PA) and antenna independently and connect them together [21]–[23]. This kind of AIAs require multiple passive networks between the PA and antenna, including the output matching network (OMN) and the harmonic tuning network (HTN) of the PA, as well as the input matching network (IMN) of the antenna. These passive networks not only occupy extra circuit areas, but also increase the insertion loss of the AIAs and therefore affect the total output power and efficiency. Furthermore, mismatch or multiple reflections may occur between the PA and the antenna if they are not matched to 50 Ω over the same operating band, which

The associate editor coordinating the review of this manuscript and approving it for publication was Vittorio Camarchia.

will deteriorate the AIA performance [24]. For example, the power-added efficiency (PAE) of a Class-E PA drops by more than 10% when it connected to a patch antenna as reported in [22]. An improved integration method is to merge the OMN of the PA into the IMN of the antenna. This has helped reduce the insertion loss of the passive networks and eliminate the mismatch between the PA and antenna [24], [25]. However, the existing passive networks of OMN and HTN still occupy a large circuit area and lower the whole PAE of the AIA. Besides, there is unwanted parasitic radiation from these passive networks [26]. This adverse effect is exacerbated due to the large power output from the PA.

Recently, a direct PA-integrated active antennas to enhance the PAE was reported in [27]. A new concept of circuit antenna was proposed in [26]. They use antennas to replace the passive networks. In other words, the antenna serves dual functions as circuit and radiator simultaneously. In this manner, the passive networks in RF front-end devices could be eliminated. So is the unwanted insertion loss, mismatch loss and parasitic radiation. Inspired by these design concepts, we propose in this paper a novel integration scheme between the Class-F PA and a slot antenna with the aim to reduce losses and increase efficiency. Different from [27], this work uses a novel slot antenna structure to achieve the impedance matching of the fundamental and harmonics. In addition, a more general design procedure, detailed loss analysis and comparison between the proposed and conventional design of AIAs are provided. These are helpful to conduct the design of high-performance AIAs. The paper is organized as follows: The losses in the conventional AIA are thoroughly analyzed in Section-II; this is followed by the detailed discussion of the integration approach and the design in Section-III; the measured results and comparisons between the conventional and proposed AIAs will be given in Section-IV; finally, the conclusion is given in Section-V.

II. LOSS ANALYSIS IN CONVENTIONAL AIA

A. LOSS FACTORS

Fig. 1 illustrates the conventional cascaded design of an AIA. The total PAE can be calculated by using equation:

$$PAE_{AIA} = \frac{P_{AIA} - P_{in}}{P_{DC}} \tag{1}$$

where P_{in} is the input power of the PA, P_{DC} is the consumed DC power by the PA, and P_{AIA} is the totally radiated power from the AIA. There are four power loss factors from the output of the PA transistor to the radiated power in free space. They are the mismatch loss between the PA transistor and the HTN/OMN (M_{L1} with a unit in dB), the insertion loss of the HTN and the OMN (I_L with a unit in dB), the mismatch loss between the HTN/OMN and the antenna (M_{L2} with a unit in dB), and the radiation efficiency of the antenna (η). Considering these loss factors, the final radiation power of the AIA can be expressed by

$$P_{AIA} = 10^{\left[\frac{P_{out}(dBm) - M_{L1}(dB) - I_L(dB) - M_{L2}(dB)}{10}\right]} \cdot \eta \tag{2}$$

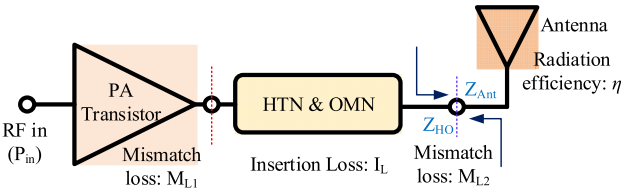

FIGURE 1. Conventional cascaded design of an AIA.

where P_{out} is the output power of the PA transistor. Increasing η and decreasing M_{L1}, I_L and M_{L2} will lead to a higher P_{AIA}, which in turn enhances the total PAE. Each part of the losses is discussed as following.

For a high-power PA transistor, the impedance requirements for optimal output power and maximal PAE are different. It usually needs a trade-off in the design. The chosen impedance also changes with the transistor state, such as the output power and the frequency, and henceforth the mismatch loss M_{L1}. The fabrication tolerance could cause further impedance mismatch.

I_L is related to the substrate, the type of HTN and OMN (e.g. lumped elements or distributed circuits) and the impedance conversion ratio [25]. To minimize the I_L, low-loss substrate, no lumped elements and low impedance conversion ratio are desired in the design.

In the conventional design, the PA and antenna are both matched to 50 Ω and connected together. M_{L2} is produced due to the imperfect matching networks or the different bandwidth of the PA and antenna. The M_{L2} can be calculated using the antenna input impedance (Z_{Ant}) and PA output impedance (Z_{HO}), as follows [28]

$$M_{L2} = 20\log_{10}\left(\sqrt{1 - \left|\frac{Z_{Ant} - Z_{HO}}{Z_{Ant} + Z_{HO}}\right|^2}\right) \tag{3}$$

Minimizing the difference between the Z_{Ant} and Z_{HO} can decrease the mismatch loss M_{L2}.

The last factor affecting the total PAE is the antenna radiation efficiency η. It is up to the substrate and antenna structure. The antenna efficiency can be estimated by the following equation [29]

$$\eta = \frac{R_r}{R_r + R_l} = \frac{G_0}{D_0} \tag{4}$$

where R_r is the radiation resistance of the antenna, R_l represents the conduction-dielectric losses, G_0 and D_0 are the maximum gain and directivity. Increasing the radiation resistance and decreasing the conduction-dielectric loss improves the antenna radiation efficiency.

From Fig. 1 and the above analyses, it can be implied that the mismatch loss M_{L1} and antenna radiation efficiency η are almost inevitable. However, the insertion loss I_L and the mismatch loss M_{L2} may be eliminated completely by re-designing the AIA structure, which is the objective of this work and will be discussed in the next section. Before that, we first examine the I_L and M_{L2} in a specific AIA design in more details.

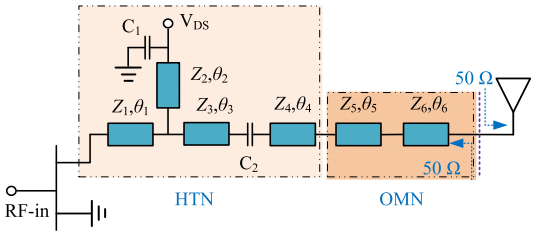

FIGURE 2. Schematic of a conventional AIA with a slot antenna.

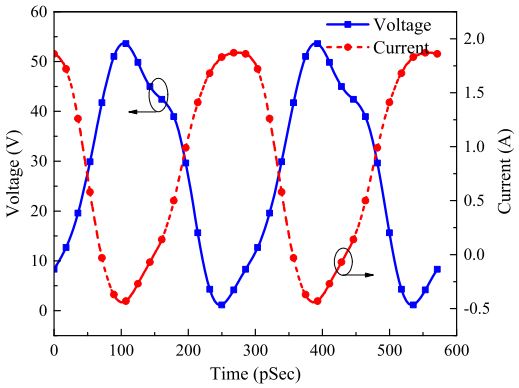

FIGURE 3. Simulated voltage and current waveforms of the PA in the conventional AIA at 3.5 GHz.

B. ANALYSIS OF I_L AND M_{L2} IN A CONVENTIONAL AIA

For demonstration, a 3.5 GHz Class-F PA cascaded with a slot antenna is designed as a high-efficiency AIA, as shown in Fig. 2. The PA and antenna are both matched to 50 Ω, and connected together to realize the AIA. GaN HEMT CGH40010F transistor from Cree Inc. is used as the power component. The DC biases of V_{DS} = 28 V and V_{GS} = −3.2V and the input power of 26 dBm are applied to the PA transistor. The substrate used is Rogers R4350B (ε_r = 3.48, tanδ = 0.002).

The HTN-OMN is designed for the PA transistor to operate at Class-F state with PAE > 50% and the output power within the equal-power circle of 2.5 dB lower from the peak output power (P_{out_max}) at 3.5 GHz. The optimized parameters are as follows: Z_1 = 33.7 Ω, θ_1 = 16.8°, Z_2 = 60.7 Ω, θ_2 = 87.9°, Z_3 = 67 Ω, θ_3 = 13.6°, Z_4 = 29.4 Ω, θ_4 = 73.1°, Z_5 = 36.3 Ω, θ_5 = 79.3°, Z_6 = 47.6 Ω, θ_6 = 20.8°, C_1 = 18 pF, C_2 = 9.9 pF. Fig. 3 shows the simulated voltage and current waveforms of the PA in the conventional AIA at the intrinsic-drain plane. Due to parasitic effects, the observed voltage and current waveforms are slightly distorted. However, they still exhibit the Class-F operation. The simulated S-parameters of the HTN - OMN is shown in Fig. 4, with the simulation model given as the inset. The load impedance of the PA transistor at 3.5 GHz with an optimal PAE (Z_S = 11.25-j6.4 Ω) is selected in this simulation. It can be seen that the insertion loss I_L is about 0.2 dB within the frequency range of 3.4-3.6 GHz.

Next, the mismatch loss M_{L2} between the Class-F PA and the antenna is analyzed. The output impedances of the

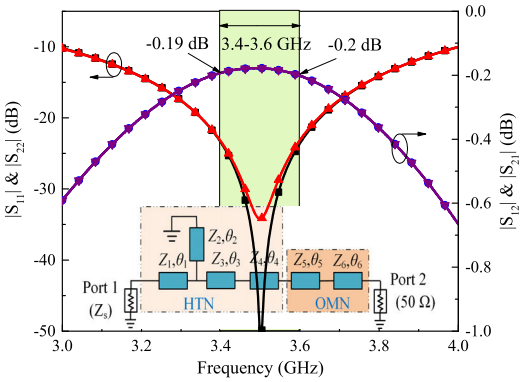

FIGURE 4. Simulated S-parameters of the HTN and OMN.

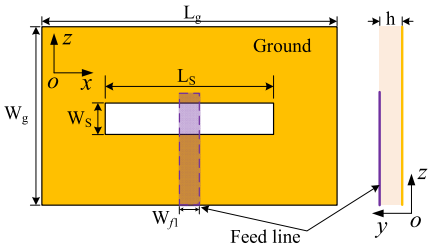

FIGURE 5. Configuration of the slot antenna (ANT A).

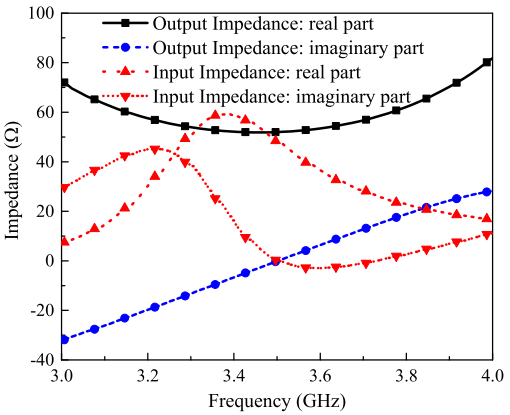

FIGURE 6. PA output and antenna input impedances as a function of frequency.

HTN - OMN and the input impedances of the slot antenna are required to calculate the mismatch loss M_{L2}. In this design, a common slot antenna (ANT A) is used for its omnidirectional radiation pattern as required by WSN applications. The layout is shown in Fig. 5, and the optimized parameters are: W_g = 32 mm, L_g = 40 mm, W_s = 3.3 mm, L_s = 23.9 mm, W_{f1} = 1.1 mm. The impedances seen at Port 2 in Fig. 4 and input impedance of ANT A are both shown in Fig. 6 as a function of frequencies. The mismatch loss M_{L2} can be calculated by using equation (3). This is shown in Fig. 7. It can be seen that the M_{L2} is nearly zero at the center frequency for this ideal case, as expected, but increases rapidly at both sides of the center frequency. Note that the PA output and antenna input reflection coefficients are both below −20 dB in this simulation. In practical circuits, the mismatch loss

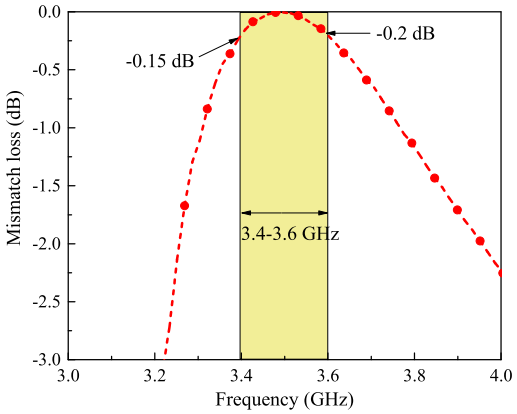

FIGURE 7. Calculated mismatch loss M_{L2} between the PA and slot antenna.

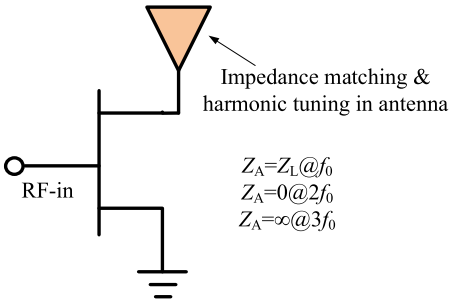

FIGURE 8. Schematic of the seamlessly integrated AIA.

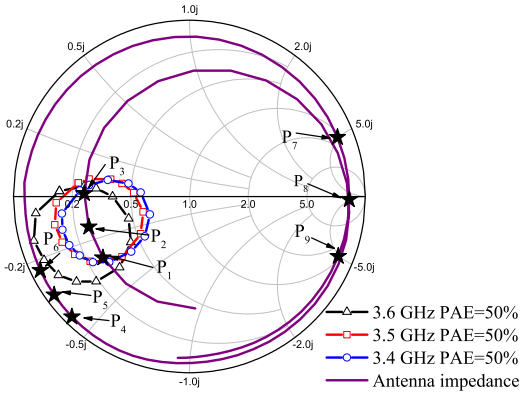

(a)

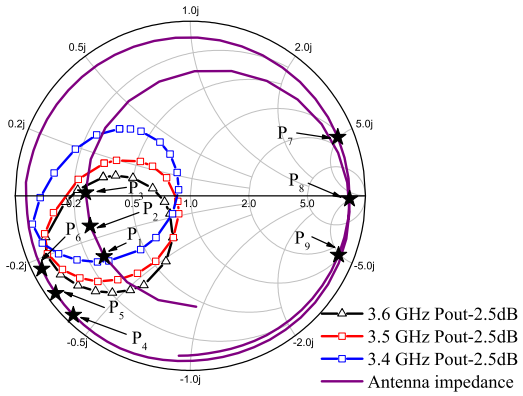

(b)

FIGURE 9. Load–pull simulation results of the PA transistor and the optimized antenna impedance at the fundamental and harmonic frequencies. (a) PAE characteristics and antenna impedance; (b) Output power characteristics and antenna impedance.

M_{L2} is commonly influenced by the uncertain impedance characteristics after fabrication. The next section will present an approach to eliminate I_L and M_{L2} by a seamless integration of the PA transistor and the antenna.

III. SEAMLESSLY INTEGRATED AIA DESIGN

We propose a seamless integration technique for AIAs to eliminate the insertion and mismatch losses (I_L and M_{L2}). The block diagram of the proposed AIA is shown in Fig. 8, where Z_A is the antenna input impedance, Z_L is the load impedance of the PA transistor, and f_0 is the fundamental operating frequency. The radiating antenna has the dual circuit functions of both impedance matching and harmonic tuning. That is $Z_A = Z_L$ at f_0 (match), $Z_A = 0$ at $2f_0$ (short), and $Z_A = \infty$ at $3\,f_0$ (open). Compared with the conventional cascaded design in Fig. 2, the two passive networks of OMN and HTN are eliminated. The mismatch loss between in PA and antenna in the conventional cascaded design (due to the imperfect impedance matching network to 50 Ω) can also be reduced. The design procedure of the seamlessly integrated AIA is as follows:

(1) Design the DC bias and stabilization circuits according to the selected PA transistor, operating frequency range and output power level;

(2) Determine the source and load impedance requirements at the fundamental and harmonics over the whole bandwidth, taking into account the desired PAE and output power level;

(3) Select and design an antenna with the objective to control its impedances at the fundamental and harmonics of the PA so that they match the PA design requirements;

(4) Design the IMN of the PA and connect the antenna to construct the seamlessly integrated AIA. The main challenge and design innovation lies with Step–(3).

The same PA transistor and substrate are utilized to realize the seamlessly integrated AIA. The operating state and DC bias of the PA transistor are also set to be the same as the conventional AIA in Section II. The design target of the AIA is a PAE of over 50% and the output power within the (P_{out_max} - 2.5 dB) circle over the frequency range of 3.4 - 3.6 GHz.

With the bias and stabilization circuits, the simulated 50% PAE and the equal-power circle of 2.5 dB below the output power are shown in Smith Chart in Fig. 9(a) and (b). The maximum PAEs and output powers at 3.4, 3.5 and 3.6 GHz are 70.2%, 73.7%, 68.5% and 38.7 dBm, 38.9 dBm, 38.5 dBm, respectively. As the design constraint of the PAE is tighter than the output power, the antenna impedance characteristics are preferentially optimized to satisfy the PAE. The optimal load impedances of the PA transistor at the maximum PAE and output power are summarized in Table I.

TABLE 1. Optimal load impedances by load pull simulation.

Frequency	For maximum PAE	For maximum output power
3.6 GHz	8.1-j9.65 Ω	9.55-j16.35 Ω
3.5 GHz	11.25-j6.4 Ω	12.45-j14.75 Ω
3.4 GHz	11.55-j5.5 Ω	13.55-j9.25 Ω

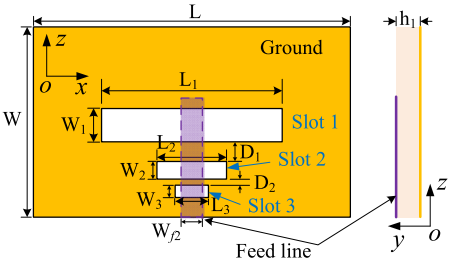

FIGURE 10. Configuration of the modified slot antenna (ANT B).

As said above, the antenna is designed to directly match the PA transistor. The input impedances of the antenna are optimized to satisfy the load impedance requirement of the transistor. Fig. 10 shows the configuration of the proposed multi-slot antenna (ANT B). Slot 1 supports the radiation at the fundamental band. Its input impedance is controlled by its length and width, as well as the dimensions of the feed line. The values of the input impedance of the antenna at the fundamental band should be inside the 50% PAE and the (P_{out_max} - 2.5 dB) circles (shown in Fig. 9). It should also approach the optimal load impedance values of the PA transistor given in Table I. The slots 2 and 3 are used to tune the harmonic responses to meet the requirements from Class-F PAs. That is that the 2nd harmonic is shorted and the 3rd harmonic is open. The impedances at the harmonic bands can be optimized by adjusting the distance (D_2) between Slot 2 and 3, when the impedances at the fundamental band is fixed. A parameter study is shown in Fig. 11. Fig. 11(a) and (b) shows the real and imaginary part of the impedances at the fundamental band, while the impedances at the 2nd and 3rd harmonic bands are shown in Fig. 11(c) and (d). It can be seen that the real and imaginary part of the impedances at the fundamental and the 2nd harmonic bands hardly change with D_2. The input impedances at the fundamental band are matched with the output of the PA transistor and the impedances at the 2nd harmonic band are close to zero. However, by changing D_2, the impedance at the 3rd harmonic band can be adjusted to achieve the open-circuit state from Fig. 11(c) and (d).

The parameters achieved after optimization are: L = 76 mm, W = 40 mm, h_1 = 0.762 mm, L_1 = 28.5 mm, W_1 = 5.3 mm, L_2 = 10.78 mm, W_2 = 2.7 mm, L_3 = 5.39 mm, W_3 = 1.93 mm, D_1 = 3.17 mm, D_2 = 1 mm, and W_{f2} = 3.4 mm. The simulated antenna impedance at the fundamental and harmonic bands are shown in Fig. 9(a) and (b) and given in Table II. P_1, P_2 and P_3 are the antenna impedances at 3.4, 3.5 and 3.6 GHz, while the P_4, P_5, P_6 and P_7, P_8, P_9 are the impedances at corresponding 2nd and 3rd harmonic frequencies. It can be seen that the impedances

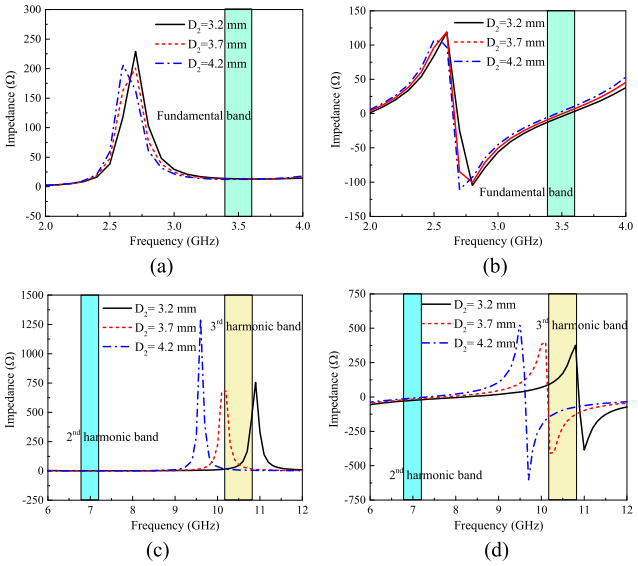

FIGURE 11. Simulated impedances at the fundamental band as a function of D_2. (a) Real and (b) imaginary parts at the fundamental band; (c) Real and (d) imaginary parts at the harmonics.

TABLE 2. Antenna impedances at each frequency.

Frequency	Impedance (Ω)
P_1 (3.4 GHz)	13.6-j14.8
P_2 (3.5 GHz)	12.9-j6.9
P_3 (3.6 GHz)	12.6+j0.7
P_4 (6.8 GHz, the 2nd harmonic of 3.4 GHz)	1.4-j21
P_5 (7.0 GHz, the 2nd harmonic of 3.5 GHz)	1.4-j16
P_6 (7.2 GHz, the 2nd harmonic of 3.6 GHz)	1.5-j11
P_7 (10.2 GHz, the 3rd harmonic of 3.4 GHz)	64.9+j243.5
P_8 (10.5 GHz, the 3rd harmonic of 3.5 GHz)	1011.2-j204.1
P_9 (10.8 GHz, the 3rd harmonic of 3.6 GHz)	60.9-j244.8

within the fundamental band are all within the 50% PAE and (P_{out_max} - 2.5 dB) circles. The impedances within the 2nd and 3rd harmonic bands are located near the short and open impedances.

It can therefore be expected that the modified slot antenna can be directly matched to the PA transistor without any HTN or OMN circuits. Fig. 12 shows the simulated voltage and current waveforms of this AIA at 3.5 GHz. These are obtained by using HFSS and ADS co-simulation. These waveforms indicate the PA transistor operates at Class-F in the proposed AIA. The seamless integration approach removes the insertion and mismatch losses in the conventional AIA, and offers high PAE over 50% with a high output power level over the frequency range of 3.4-3.6 GHz.

IV. RESULTS AND DISCUSSION

For comparisons, both the conventional and the seamless integrated AIAs are designed, fabricated and measured. The photographs of these prototypes are shown in Fig. 13. The size of the seamlessly integrated AIA is 76 mm × 40 mm. Compared to the conventional design, more than 30% size reduction is achieved.

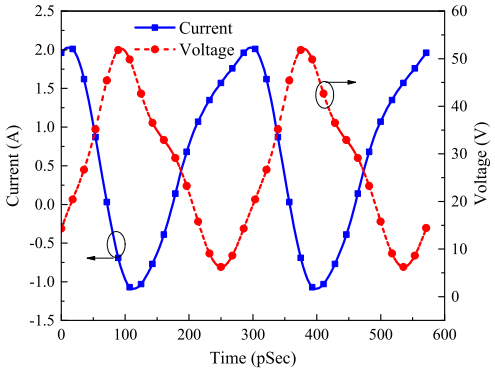

FIGURE 12. Simulated voltage and current waveforms of seamless integrated AIA.

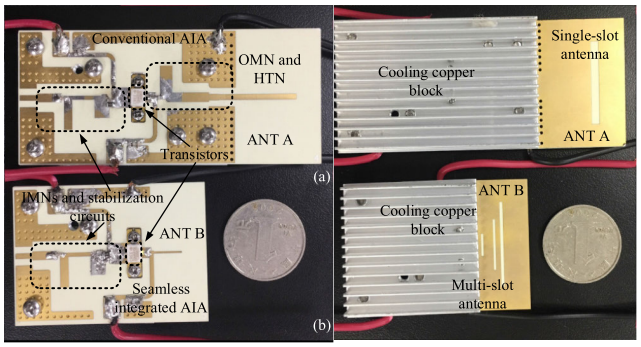

FIGURE 13. Photographs of (a) the conventional AIA and (b) the seamlessly integrated AIA.

The test procedure contains three steps: the first step uses a reference antenna cascaded with a pre-amplifier to drive the power amplifier in the conventional and seamless integrated AIAs. The purpose of this step is to calibrate the path loss and remove the influence of the pre-amplifier. Then the reference antenna is replaced by the device under test to measure the active gain (G_{act}) of the AIA. The third step is to remove the pre-amplifier and do the calibration again with the reference antenna. After that, the ANT A and B are measured. Considering the effect of large ground plane and cooling copper block (with a thickness of 5 mm) on the radiation patterns, the ANT A and B are both attached to the same size ground and cooling blocks as used in the two AIAs. The detailed measurement setup and procedures follow those in [27]. The Satimo SG-24 antenna test system from MVG is used to test the two AIAs, ANT A and B.

Based on the known input RF power (P_{in}) to the AIA, the measured active gain (G_{act}) of the AIA and the measured gain (G_{ant}) of the corresponding separated antenna (ANT A or B), the effective isotropic radiated power (EIRP) and output RF power of the proposed AIAs can be calculated as:

$$EIRP\,(dBm) = P_{in}\,(dBm) + G_{act}\,(dBi) \quad (5)$$

$$P_{AIA}\,(dBm) = EIRP\,(dBm) - G_{ant}\,(dBi) \quad (6)$$

With the DC consumption power (P_{DC}), the PAE of the AIA can be calculated using equation (1).

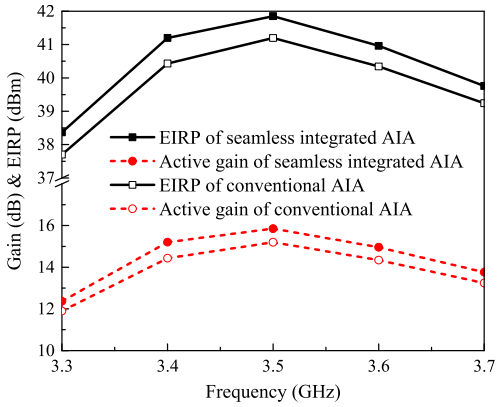

FIGURE 14. Measured EIRP and gain at an input power of 26 dBm.

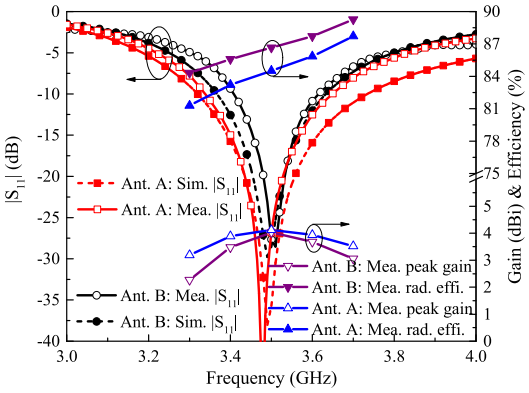

FIGURE 15. Comparisons of the two slot antennas.

The measured active gains, EIRPs of the seamless integrated and the conventional AIAs are shown in Fig. 14. The EIRP is measured with the input power of 26 dBm and it is over 38.4 dBm over the frequency range of 3.3-3.7 GHz for the seamless integrated AIA. The active gain is more than 12.4 dB over the same frequency range and the maximum gain is 15.9 dB at 3.5 GHz. For the conventional design, the measured EIRP and active gain are about 0.5-0.8 dB lower than the seamless integrated one. This is mainly attributed to the elimination of insertion and mismatch losses in the seamless integrated AIA, as well as the slight gain difference between ANT A and B. The measured results of the two separated antennas (ANT A and B) are shown in Fig. 15. It should be noted that the ANT B is re-matched to 50 Ω to facilitate measurement and comparison. The radiation efficiency (η) difference between these two slot antennas is within 2.6% over 3.3-3.7 GHz. This shows the losses related to η are similar for the two slot antennas. The peak gain of ANT A in the conventional AIA is about 0.7 dB higher than the ANT B in the seamless AIA at 3.3 GHz, mainly because ANT A has a better measured $|S_{11}|$. Within the bandwidth of 3.4-3.6 GHz, the difference in gain between the two slot antennas is less than 0.2 dB.

According to the equations (6) and (7), the measured large-signal performances of the seamless integrated AIA

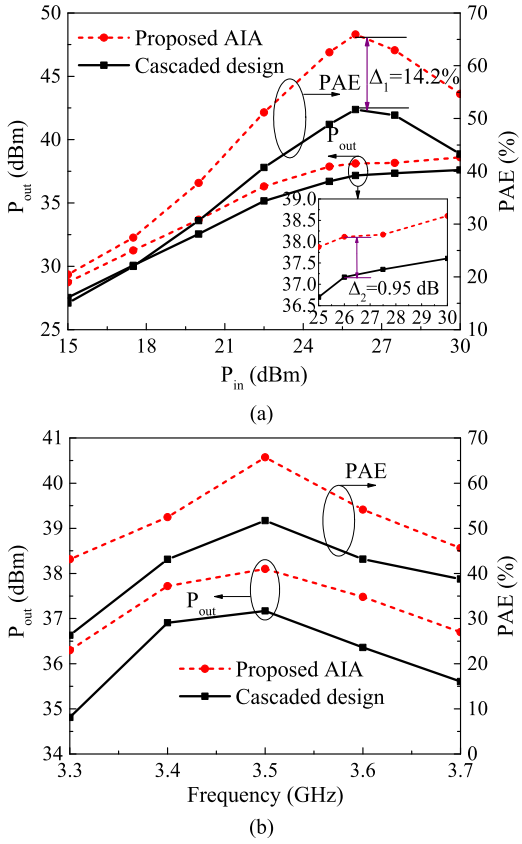

FIGURE 16. Measured extrapolated large-signal characteristics. (a) PAE and output power versus input power at 3.5 GHz; (b) PAE and output power versus frequency at input power of 26 dBm.

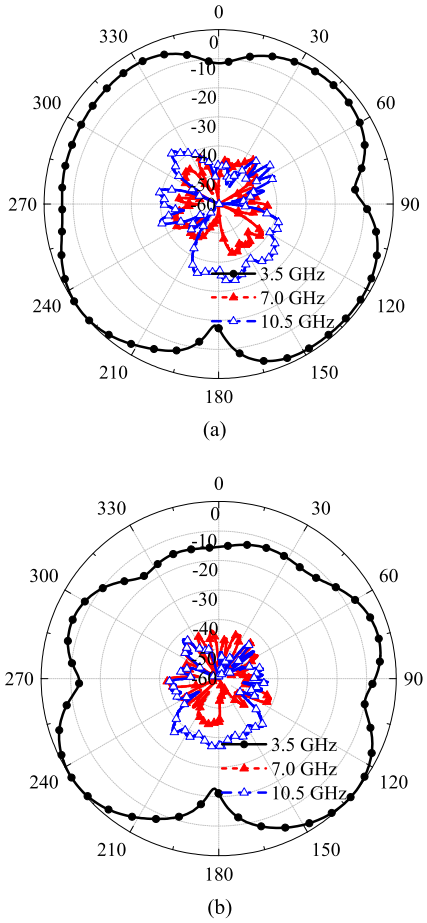

FIGURE 17. Measured normalized radiation patterns of the proposed AIA. (a) *xz*-plane, (b)*yz*-plane.

and conventional AIA are compared in Fig. 16. At 3.5 GHz, the maximum PAEs are 65.9% and 51.7% with an input power of 26 dBm, as shown in Fig. 16(a). This is an increase of over 14%. At this input power, the output powers are 38.1 dBm and 37.2 dBm, respectively. The measured PAEs and output powers as a function of frequency of the two designs are shown in Fig. 16(b). Over the tested frequency range of 3.3-3.7 GHz, the PAE and output power of the conventional AIA are consistently lower than the seamless integrated one. The PAE of the seamless integrated AIA is over 52 % and the output power higher than 37.5 dBm over 3.4-3.6 GHz. The maximum PAE of 65.9 % and output power of 38.1 dBm occur at 3.5 GHz.

Compared with the conventional AIA, the output power of the seamless integrated AIA is about 0.95 dB higher at 3.5 GHz with the input power of 26 dBm. The corresponding PAE of the AIA is about 14.2% higher. As stated above, this is mainly attributed to the elimination of insertion and mismatch losses and the slight difference in radiation efficiencies between ANT A and ANT B.

Fig. 17 shows the measured normalized radiation patterns of the seamless integrated AIA at 3.5 GHz, 7.0 GHz and 10.5 GHz, respectively. This measurement is carried out at the input power of 26 dBm and 3.5 GHz. The radiation patterns at 3.5 GHz are distorted due to the proximity of the large ground plane and cooling copper block at the back side of the PA. The spurious radiations at the second and third harmonic of the proposed structure are suppressed by over 30 dB in all directions.

TABLE 3. Comparison of active antennas integrated with high efficiency PA.

Ref.	Transistor	Freq. (GHz)	PAE peak (%)	Pout (dBm)	EIRP (dBm)	Integration method
[22]	GaAs	2	>60	21.7	39.7*	Directly cascaded
[25]	GaN	5.8	59.9	38.2	44.6	Improved OMN
[27]	GaAs	20	34.8	24.7	30.7	directly integrated
This work	GaN	3.5	51.7	37.2	41.2	Directly cascaded
This work	GaN	3.5	65.9	38.1	41.9	Seamless integration

*ERP of the 2×2 active array antenna.

The comparison of our work with other AIAs with high efficiency PA is given in Table III. Because of the elimination of the passive networks from the output of the Class-F PA and the mismatch between the PA and antenna, the proposed design successfully achieved a seamless integration with a

competitively high PAE and output power compared with other work.

V. CONCLUSION

This work presented a technique to reduce the loss in AIA design by a seamless integration approach. The OMN and HTN in the conventional Class-F PA are eliminated and absorbed by an optimized multi-functional slot antenna. Thus, the output of the PA transistor is connected with the antenna directly without any passive network in between. Because of the elimination of these passive networks and the associated losses, the PAE and output power are improved with a more compact circuit size. The comparisons between the conventional and seamless integrated AIAs demonstrated the advantage of the proposed integration scheme and verify the proposed design method. The proposed integration technique is a good candidate for high-efficiency transmitter front-ends in wireless systems such as MPT or communications.

REFERENCES

[1] Z. Popovic, E. A. Falkenstein, D. Costinett, and R. Zane, "Low-power far-field wireless powering for wireless sensors," *Proc. IEEE*, vol. 101, no. 6, pp. 1397–1409, Jun. 2013.
[2] Z. Wang, L. Duan, and R. Zhang, "Adaptively directional wireless power transfer for large-scale sensor networks," *IEEE J. Sel. Areas Commun.*, vol. 34, no. 5, pp. 1785–1800, May 2016.
[3] M. Chen, M. Wang, and H. Yu, "A self-powered 3.26-mW 70-m wireless temperature sensor node for power grid monitoring," *IEEE Trans. Ind. Electron.*, vol. 65, no. 11, pp. 8956–8965, Nov. 2018.
[4] H. Zhang, Y.-X. Guo, Z. Zhong, and W. Wu, "Cooperative integration of RF energy harvesting and dedicated WPT for wireless sensor networks," *IEEE Microw. Wireless Compon. Lett.*, vol. 29, no. 4, pp. 291–293, Apr. 2019.
[5] E. A. U. Calpa, A. U. A. Florian, F. Ramirez, J. S. Riquelme, J. C. B. Reyes, and F. E. Segura-Quijano, "Towards fully integrated low-cost inductive powered CMOS wireless temperature sensor," *IEEE Trans. Ind. Electron.*, vol. 64, no. 11, pp. 8718–8727, Nov. 2017.
[6] Y. Yang, C. Wang, and J. Li, "Power sensor networks by wireless energy—Current status and future trends," in *Proc. Int. Conf. Comput., Netw. Commun. (ICNC)*, Garden Grove, CA, USA, 2015, pp. 648–652.
[7] H.-W. Zhou, X.-X. Yang, and S. Rahim, "Array synthesis for optimal microwave power transmission in the presence of excitation errors," *IEEE Access*, vol. 6, pp. 27433–27441, 2018.
[8] S. Sasaki, K. Tanaka, and K.-I. Maki, "Microwave power transmission technologies for solar power satellites," *Proc. IEEE*, vol. 101, no. 6, pp. 1438–1447, Jun. 2013.
[9] X. Yi, X. Chen, L. Zhou, S. Hao, B. Zhang, and X. Duan, "A microwave power transmission experiment based on the near-field focused transmitter," *IEEE Antennas Wireless Propag. Lett.*, vol. 18, no. 6, pp. 1105–1108, Jun. 2019.
[10] V.-H. Duong, N. X. Hieu, H.-S. Lee, and J.-W. Lee, "A battery-assisted passive EPC Gen-2 RFID sensor tag IC with efficient battery power management and RF energy harvesting," *IEEE Trans. Ind. Electron.*, vol. 63, no. 11, pp. 7112–7123, Nov. 2016.
[11] J. J. Estrada-Lopez, A. Abuellil, A. Costilla-Reyes, M. Abouzied, S. Yoon, and E. Sanchez-Sinencio, "A fully integrated maximum power tracking combiner for energy harvesting IoT applications," *IEEE Trans. Ind. Electron.*, vol. 67, no. 4, pp. 2744–2754, Apr. 2020.
[12] C. H. P. Lorenz, S. Hemour, W. Li, Y. Xie, J. Gauthier, P. Fay, and K. Wu, "Breaking the efficiency barrier for ambient microwave power harvesting with heterojunction backward tunnel diodes," *IEEE Trans. Microw. Theory Techn.*, vol. 63, no. 12, pp. 4544–4555, Dec. 2015.
[13] Y. Yamashita, T. Nakada, T. Kumamoto, R. Suzuki, and M. Tanabe, "X-band GaN HEMT advanced power amplifier unit for compact active phased array antennas," in *Proc. ICCAS-SICE Int. Joint Conf.*, Aug. 2009, pp. 3047–3050.
[14] H. Seita and S. Kawasaki, "Compact and high-power, spatial power combiner by active integrated antenna technique at 5.8 GHz," *IEICE Trans. Electron.*, vol. E91-C, no. 11, pp. 1757–1764, Nov. 2008.
[15] M. V. Ivashina, "Joint design and co-integration of antenna-IC systems," in *Proc. 13th Eur. Conf. Antennas Propag. (EuCAP)*, Krakow, Poland, 2019, pp. 1–7.
[16] S. B. Sharma, S. C. Bera, and S. B. Chakraborty, "Active antenna for improved efficiency and reduced harmonic radiation," *Int. J. Electron.*, vol. 95, no. 2, pp. 85–98, Feb. 2008.
[17] E. Lee, K. M. Chan, P. Gardner, and T. E. Dodgson, "Active integrated antenna design using a contact-less, proximity coupled, differentially fed technique," *IEEE Trans. Antennas Propag.*, vol. 55, no. 2, pp. 267–276, Feb. 2007.
[18] C.-H. Wu and T.-G. Ma, "Miniaturized self-oscillating active integrated antenna with quasi-isotropic radiation," *IEEE Trans. Antennas Propag.*, vol. 62, no. 2, pp. 933–936, Feb. 2014.
[19] H. T. Nguyen, T. Chi, S. Li, and H. Wang, "A linear high-efficiency millimeter-wave CMOS doherty radiator leveraging multi-feed on-antenna active load modulation," *IEEE J. Solid-State Circuits*, vol. 53, no. 12, pp. 3587–3598, Dec. 2018.
[20] A. Khoshniat, T. Yekan, R. Baktur, and K. F. Warnick, "Active integrated antenna supporting linear and circular polarizations," *IEEE Trans. Compon., Packag., Manuf. Technol.*, vol. 7, no. 2, pp. 238–245, Feb. 2017.
[21] Y. Chung, C. Y. Hang, S. Cai, Y. Qian, C. P. Wen, K. L. Wang, and T. Itoh, "AlGaN/GaN HFET power amplifier integrated with microstrip antenna for RF front-end applications," *IEEE Trans. Microw. Theory Techn.*, vol. 51, no. 2, pp. 653–659, Feb. 2003.
[22] Y. Qin, S. Gao, and A. Sambell, "Broadband high-efficiency linearly and circularly polarized active integrated antennas," *IEEE Trans. Microw. Theory Techn.*, vol. 54, no. 6, pp. 2723–2732, Jun. 2006.
[23] Y. Song, Y. Wu, J. Yang, Y. Tian, W. Tong, Y. Chen, C. Wang, X. Tang, J. Benedikt, and K. Kang, "A compact ka-band active integrated antenna with a GaAs amplifier in a ceramic package," *IEEE Antennas Wireless Propag. Lett.*, vol. 16, pp. 2416–2419, 2017.
[24] S. K. Dhar, M. S. Sharawi, O. Hammi, and F. M. Ghannouchi, "An active integrated ultra-wideband MIMO antenna," *IEEE Trans. Antennas Propag.*, vol. 64, no. 4, pp. 1573–1578, Apr. 2016.
[25] N. Hasegawa and N. Shinohara, "C-band active-antenna design for effective integration with a GaN amplifier," *IEEE Trans. Microw. Theory Techn.*, vol. 65, no. 12, pp. 4976–4983, Dec. 2017.
[26] S. N. Nallandhigal and K. Wu, "Unified and integrated circuit antenna in front End—A proof of concept," *IEEE Trans. Microw. Theory Techn.*, vol. 67, no. 1, pp. 347–364, Jan. 2019.
[27] W.-C. Liao, R. Maaskant, T. Emanuelsson, V. Vassilev, O. Iupikov, and M. Ivashina, "A directly matched PA-integrated K-band antenna for efficient mm-Wave high-power generation," *IEEE Antennas Wireless Propag. Lett.*, vol. 18, no. 11, pp. 2389–2393, Nov. 2019.
[28] D. M. Pozar, *Microwave Engineering*. New York, NY, USA: Wiley, 2006.
[29] C. A. Balanis, *Antenna Theory Analysis and Design*, 3rd ed. New York, NY, USA: Wiley, 2005.

YUNLONG LU received the B.S. degree in electronic engineering from Ningbo University, Ningbo, China, in 2007, and the M.S. and Ph.D. degrees in electronic engineering from Zhejiang University, Hangzhou, China, in 2010 and 2015, respectively. From July 2008 to December 2008, he was a Research Assistant with Nanyang Technological University, Singapore. From September 2018 to September 2019, he was a Visiting Scholar with the Poly-Grames Research Center, École Polytechnique de Montréal, University of Montreal, Montreal, QC, Canada. He is currently working as an Associate Professor with the Faculty of Electrical Engineering and Computer Science, Ningbo University. His research interests include microwave/millimeter-wave circuit integration and devices, antenna arrays, and multiport filtering networks.

QING LIU received the B.S. degree in electronic and information engineering from Liaoning Science and Technology University, Anshan, China, in 2018. He is currently pursuing the M.S. degree in electronics and communication engineering with Ningbo University, Ningbo, China. His current research interests include microwave and radio frequency circuits, and antenna.

YI WANG (Senior Member, IEEE) was born in Shandong, China. He received the B.Sc. degree in physics and the M.Sc. degree in condensed matter physics from the University of Science and Technology, Beijing, China, in 1998 and 2001, respectively, and the Ph.D. degree in electronic and electrical engineering from the University of Birmingham, Birmingham, U.K., in 2005. In 2011, he became a Senior Lecturer and then a Reader with the University of Greenwich. In 2018, he joined the University of Birmingham as a Senior Lecturer. His current research interests include millimeter-wave and terahertz devices for metrology, communications and sensors, micromachining, microwave circuits based on multiport filtering networks, and filter-antenna integration.

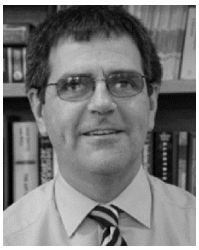

PETER GARDNER (Senior Member, IEEE) received the B.A. degree in physics from the University of Oxford, Oxford, U.K., in 1980, and the M.Sc. and Ph.D. degrees in electrical engineering and electronics from The University of Manchester Institute of Science and Technology, Manchester, U.K., in 1990 and 1992, respectively. He is currently a Professor of microwave engineering, the Head of the Department of Electronic, Electrical, and Systems Engineering, and the Head of the Communication and Sensing Research Group, University of Birmingham, Birmingham, U.K. He was appointed as a Lecturer with the University of Birmingham, in 1994, where he became a Professor, in 2015. His research interests include the theory, technology, and applications of the RF, microwave, millimeter-wave, and THz bands.

WANG HE received the B.S. degree in communication engineering from Xi'an Shiyou University, Xi'an, China, in 2016, and the M.S. degree in communication and information system from Ningbo University, Ningbo, China, in 2019. His current research interests include antenna and RF circuits.

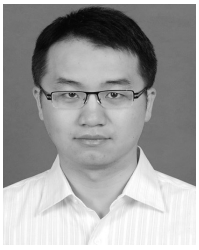

YI CHEN was born in Ningbo, China. He received the Dipl.Ing. degree from the Karlsruhe Institute of Technology, Karlsruhe, Germany, in 2011, and the Dr.Ing. degree from the University of Hannover, Hannover, Germany, in 2017. He is currently a Lecturer with the Faculty of Electrical Engineering and Computer Science, Ningbo University, Ningbo, China. His current research interests include reconfigurable mobile terminal antennas and MEMS for high-frequency technologies.

JIFU HUANG received the B.S. and M.S. degrees in radio engineering from Southeast University, China, in 1982 and 1987, respectively, and the Ph.D. degree in electrical and computer engineering from the University of Victoria, Canada, in 1995. From 1982 to 1991, he was a Lecturer with Southeast University. From 1991 to 1994, he was a Research Assistant with the Department of Electrical Engineering, University of Victoria. From 1994 to 1995, he worked as a Postdoctoral Fellow with the Research Center for Advanced Microwave and Space Electronics, École Polytechnique of Montreal, Canada. From 1995 to 2015, he joined the industry at Harris, M/A-COM, Telebeam, 2Wire, and ZTE Inc., USA, as a Senior Microwave Engineer to Principal Microwave Engineer. In 2015, he was appointed as a Professor with Ningbo University, China. His research interests include the microwave and millimeter-wave theory, engineering, and applications.

TAIJUN LIU (Senior Member, IEEE) received the B.S. degree in applied physics from the China University of Petroleum, Dongying, China, in 1986, the M.Eng. degree in electrical engineering from the University of Electronic Science and Technology of China, Chengdu, China, in 1989, and the Ph.D. degree from the École Polytechnique de Montréal, University of Montreal, Montreal, QC, Canada, in 2005. He is currently a Professor with the Faculty of Electrical Engineering and Computer Science, Ningbo University, Ningbo, China. His current research interests include nonlinear modeling and linearization of wideband transmitters/power amplifiers, and the design of ultralinear high-efficiency intelligent power amplifiers for broadband wireless and satellite communication systems.